Journal of Materials Science: Materials in Electronics (2020) 31:3312–3322
https://doi.org/10.1007/s10854-020-02879-w

Radiation tolerance, charge trapping, and defect dynamics studies of ALD-grown Al/HfO_2/Si nMOSCAPs

N. Manikanthababu[1,2] · T. Basu[3] · S. Vajandar[4] · S. V. S. Nageswara Rao[2,5] · B. K. Panigrahi[1,6] · T. Osipowicz[4] · A. P. Pathak[2,7]

Received: 9 June 2019 / Accepted: 6 January 2020 / Published online: 16 January 2020
© Springer Science+Business Media, LLC, part of Springer Nature 2020

Abstract

The radiation response, long-term performance, and reliability of HfO_2-based gate dielectric materials play a critical role in metal oxide semiconductor (MOS) technology for space device applications. Al/HfO_2/Si atomic layer-deposited devices were irradiated by gamma and swift heavy ions. An increase in the leakage current and charge trapping has been observed as the gamma irradiation dose varied from 25 to 100 krad. The density of oxide traps is found to increase with an increase in the gamma dose while the interface trap density is found to decrease. Another set of samples were irradiated by 120 MeV Au ions to study the SHI-induced defect annealing/creation of defects and intermixing effects in HfO_2/Si-based devices. The formation of an interfacial layer of HfSiO at a fluence of at 5×10^{13} cm^{-2} is revealed by X-ray reflectivity analysis. The densities of interface- and oxide-trapped charges are found to decrease up to a critical fluence of 1×10^{12} cm^{-2} and then increase with further increase in fluence to 5×10^{13} cm^{-2}. The presence of the interlayer, due to the swift heavy ion-induced intermixing, has been confirmed by X-ray photoelectron spectroscopy measurements. Various current conduction mechanisms in both substrate and gate injection cases were used to understand the basic mechanisms of direct, Fowler–Nordheim, and Poole–Frenkel tunneling, as well as Schottky emission in these devices. These studies elucidated the radiation tolerance and charge-trapping behavior of Al/HfO_2/Si nMOS capacitors.

1 Introduction

The enactment of new-generation gate dielectric materials as insulators in complementary metal oxide semiconductor (CMOS) technology is essential to accomplish radiation-tolerant and reliable space electronics [1]. Consequently, there is a pre-requisite to comprehend the response of these materials to radiation exposure, in order to test and develop radiation-tolerant devices [2]. Advanced CMOS devices used in space electronics are expected to be hampered by the prevailing harsh radiation environment [3, 4]. Certain changes may occur in the operation of these devices, such as communication, imaging, control, and power consumption [5]. Moreover, long-term degradation produced by incessant exposure may cause transient or a catastrophic device failure [6]. The study of new-generation high-k dielectrics in radiation environment is of current interest due to their prospective improvements in the operative lifetimes and enhanced performance compared to traditional SiO_2 gate dielectric materials [7–10]. New-generation high-k dielectric materials such as HfO_2, Al_2O_3, ZrO_2, Y_2O_3, TiO_2, and Ta_2O_5 and/or the silicates/oxynitrides have already been introduced by the

✉ N. Manikanthababu
maniphysics07@gmail.com

✉ A. P. Pathak
anandp5@yahoo.com

1 Materials Science Group, Indira Gandhi Centre for Atomic Research, Kalpakkam 603102, India

2 School of Physics, University of Hyderabad, Hyderabad 500046, India

3 Centre for Advanced 2D Materials (CA2DM), National University of Singapore, Singapore 117542, Singapore

4 Department of Physics, Centre for Ion Beam Applications (CIBA), National University of Singapore, Singapore 117542, Singapore

5 School of Physics, Centre for Advanced Studies in Electronics Science and Technology (CASEST), University of Hyderabad, Hyderabad 500046, India

6 Electronics and Instrumentation Group, Indira Gandhi Center for Atomic Research, Kalpakkam 603102, India

7 Department of Physics, Sikkim University, Gangtok 737102, India

semiconductor industry to reduce the leakage currents as the gate oxides are designed few nanometers to improve device performance further [11–14]. HfO_2 has outperformed all the other materials as it has high dielectric constant (~25) with a moderate band gap (5.8 eV) and acceptable band-offsets with Si and its stable thermal and chemical compatibility on Si surface [15–17]. There are numerous reports on the fabrication of HfO_2-based devices [18–21]. Mostly, atomic layer deposition (ALD) technique has been used owing to its precise control over thickness, stoichiometry, low trap density, and uniformity [22, 23]. Here, it is important to note that the HfO_2 films deposited by other methods, like radio frequency magnetron sputtering or electron beam evaporation may exhibit different charge-trapping behavior because of the differences in uniformity of the film, pre-existing trap densities, bonding states, etc. [24, 25]. If HfO_2-based high-k gate dielectric materials are to be used as fundamental components of metal oxide semiconductor (MOS) devices in terrestrial applications, their radiation response will play a crucial role in the device operation and performance, which needs to be understood prior to their experimentation [26–28]. However, only few reports are available on the radiation response of the HfO_2-based high-k dielectric materials and further studies will provide the practical implications to understand their radiation response/damage [29–31].

Not much has been published on swift heavy ion (SHI) irradiation of HfO_2-based MOS capacitors, compared with the extensive literature on irradiation of SiO_2. The latter has clearly improved the understanding of commonly observed intrinsic defects in the MOS device structures.

Consequently, the generation, evolution, and annealing of processing related, as well as radiation-induced, defects have to be understood in a typical high-k-based MOS device configuration. It was reported that heavy ion irradiation can induce leakage current, breakdown, and reduce the lifetime of ultrathin oxide films. Ionizing radiation exposure of metal oxide semiconductor (MOS) devices can alter their electrical performance, sometimes leading to a permanent failure due to continuous exposure to radiation and temporary effects occurring from a transient high-energy particle radiation, viz. single-event effects, are some of the most commonly studied device failure mechanisms in the domain of radiation effects and reliability. Charge trapping, defect dynamics, and leakage current conduction mechanisms are critical to study the effects of SHI irradiation.

Gamma rays interact with the material through the photoelectric effect, Compton scattering, or pair production depending on the incoming gamma energy. In general, the gamma rays interact with electrons of the material and the energy eventually will be transferred to the lattice via electron–phonon coupling and cause ionization. In the process of ionization, electron–hole pairs (EPSs) will be generated in dielectric materials [32]. A part of the electrons and holes will recombine with each other and the rest will diffuse and transport though the material, if there is a bias voltage. As the dose of irradiation increases, the devices will gradually degrade and fail when the total dose is sufficiently large. This phenomenon is called total dose effect. ^{60}Co gamma rays with the average energy of 1.25 MeV will interact with the material largely by Compton effect, creating EHPs which can be separated and be made mobile by the electric field due to applied gate voltage. However, the movement of these charges either can be towards the metal contact through the gate oxide or can be hindered or clogged entirely by the trapping at defects in the gate oxide. These defects can be vacancies, interstitials, or dangling bonds which can be positively or negatively charged. This trapping of mobile charges may ultimately affect the electrical properties (I–V and C–V) of MOS devices [33]. Gamma rays are much less likely to cause structural or morphological damage than SHIs, because collisional direct damage to the lattice does not occur. High-energy heavy ions, familiarly known as SHIs, have energy ranging from few tens of MeV to few GeV and lose energy to the target (≥ 1 MeV/amu) primarily via inelastic collisions with the target material [34]. These projectile ions impart their energy to the electron cloud and these electrons in turn transfer their energy to the lattice via electron–phonon interactions. This is known as 'electronic energy loss' $(dE/dx)_e$. In this case, the nuclear energy loss $(dE/dx)_n$ is negligible as compared to the electronic energy loss [35, 36]. Intense electronic energy deposition can be effectively used to modify material properties. Copious studies have been reported on structural phase transformation, electrical and optical properties of various metals, semiconductors, and insulator-based Schottky and MOS devices induced by SHI irradiation [37–41]. The high electronic energy deposition leads to various changes in the devices including defects annealing/creation and interface mixing depending upon the energy of the projectile and fluence. SHI irradiation can produce point defects which can be either vacancies or interstitials. However, the trap-rich characteristic of high-k dielectric materials, oxide, and interface defects can play crucial role in the leakage current conduction mechanism [42]. Unlike gamma irradiation, SHI irradiation can produce high density of localized point defects in the devices [43]. The low density of defects produced by gamma irradiation can effectively vary the electrical characteristics of the devices. However, these changes prompted by gamma irradiation are more prominent as compared to those induced by single energy ion irradiation of analogous fluence. These changes can lead to either electron or hole trapping. The present work is carried out on the ALD-grown samples at relatively low doses starting from 25 to 100 krad to understand their radiation tolerance and charge-trapping properties. The objective is to study probable interaction mechanisms in gamma, SHI irradiation in $Al/HfO_2/Si$ n-channel

metal oxide semiconductor capacitors (nMOCAPs) to test the device tolerance and sustenance. Comparison between the effects caused by gamma and SHI in the technologically important devices has been presented.

2 Experimental

5 nm HfO_2 thin films were grown by ALD using standard TEMA-Hf (tetrakis-ethylmethylamino hafnium) precursors with ozone, pulsed alternatively, deposited at 460 °C, 4–8 torr pressure, and growth rate was as low as 0.5 A/min. The ALD reactor used in our experiment was a four-chamber QXP platform at Aixtron Inc., USA. Al (a dot of radius 0.5 mm) has been used as a top electrode and Ag paste along with the help of an Al foil was used as a backside contact of Si. "Al (50 nm)/HfO_2(5 nm)/p-Si" device structure has been shown in the Fig. 1 (inset). Bruker D8 Discover diffractometer (Cu-K_α source (1.5406 Å) was used for X-ray reflectivity (XRR) measurements (glancing angle was 0.4^0). These samples were then subjected to gamma irradiation by using a ^{60}Co gamma (1.25 MeV γ) source (1200 Gamma chamber available at Inter University Accelerator Center (IUAC), New Delhi, India). Gamma irradiation was performed on all the samples with a constant dose rate of 460 krad/h. The samples were irradiated at various doses ranging from 25 and 100 krad. Room temperature 120 MeV Au ion irradiation was performed at IUAC, New Delhi, in a high-vacuum chamber ($<10^{-6}$ mbar) at a constant beam current of one particle nano-Ampere (~ 1 pnA). The beam (of 1 mm diameter) was uniformly scanned over 1 × 1 cm on the sample surface using magnetic scanners to achieve uniform irradiation profiles. I–V (leakage current) and C–V measurements were performed using an in-house

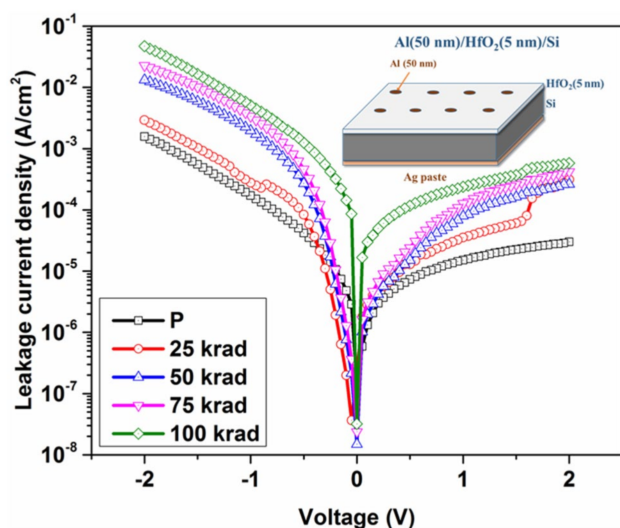

Fig. 1 I–V characteristics of pristine and gamma-irradiated samples (inset: Device structure)

Agilent technologies B1500A semiconductor device analyzer. The applied bias voltage ranges from −5 to +5 V, and C–V measurements were performed at a frequency of 1 MHz. X-ray photoelectron spectroscopy (XPS: Omicron instruments) measurements were performed at Surface Science Laboratory, NUS, equipped with a Mg K_α source ($h\nu = 1253.6$ eV) and hemispherical analyser. The data have been fitted with CasaXPS software [44].

3 Results and Discussion

In order to systematically study the radiation response of HfO_2/Si devices, the samples were divided into two sets. One set of the samples was used for gamma irradiation and the other set was used for SHI (120 MeV Au) irradiation. The Tables 1 and 2 provide the estimates of the number of defects produced by gamma and ion irradiation in HfO_2 samples, respectively. The number of defects and atomic displacements produced by ion irradiation in HfO_2/Si samples was estimated by [45, 46] Stopping Range of Ions in Matter simulation (SRIM) simulations [47]. The dose (rad) is given by [48]

$$\text{Dose} = \frac{1.6 \times 10^{-6} \times \left(\frac{\mathrm{d}E}{\mathrm{d}x}\right)_e \times \phi}{\rho_{\mathrm{HfO}_2}} \tag{1}$$

where $(\mathrm{d}E/\mathrm{d}x)_e$ is the electronic energy loss obtained from SRIM calculations, ϕ is the irradiation fluence, and ρ is the density of HfO_2 (9.68 g/cm^3).

The pristine sample has been characterized by XRR measurements which provided the estimates of the thickness

Table 1 Gamma irradiation-induced atomic displacements in HfO_2 and its equivalent ion fluence

Gamma irradiation dose (krad)	Estimated number of displacements/cm^2	Equivalent ion fluence (Au$^+$ cm^{-2})
25	0.288	5.36×10^7
50	0.576	1.07×10^8
75	1.15	1.61×10^8
100	2.30	2.14×10^8

Table 2 Ion irradiation-induced atomic displacements in HfO_2 and its equivalent absorption dose

Ion irradiation fluence (cm^{-2})	Estimated number of displacements/cm^2	Equivalent Gamma irradiation dose (krad)
1×10^{11}	2.67×10^2	4.67×10^4
1×10^{12}	2.67×10^3	4.67×10^5
1×10^{13}	2.67×10^4	4.67×10^6
5×10^{13}	1.33×10^5	2.33×10^7

Table 3 Film parameters estimated by XRR analysis

120 MeV Au ion & fluence (cm^{-2})	Thickness (nm)		Surface roughness (nm)	Interface roughness (nm)
	HfO_2	HfSiO	HfO_2	HfO_2/HfSiO
Pristine	4.93 ± 0.3	–	0.14 ± 0.06	–
Irradiated (fluence: 5×10^{13})	3.89 ± 0.4	2.12 ± 0.6	0.39 ± 0.04	0.08 ± 0.03

of each layer and surface/interface roughness. The thickness of the interlayers of the pristine sample (P) is presented in Table 3 by considering the standard density of HfO_2 (9.68 g/cm^3).

3.1 Gamma irradiation studies

HfO_2/Si pristine and all the irradiated samples were characterized by XRR measurements. However, as expected, there are no significant structural changes observed between pristine and irradiated samples.

The pre-irradiation electrical measurements are very important as they reveal the intrinsic characteristics of the devices such as charge trapping and flat-band voltage shift. I–V and frequency (1 MHz) C–V measurements were performed as a pre-characterization for all the devices. These measurements were performed at room temperature, aimed to extract leakage current density, oxide-, and interface-trapped charge densities before and after gamma irradiation with doses of 25, 50, 75, and 100 krad. The leakage current is found to increase with increase in the irradiation dose (Fig. 1). The current conduction mechanisms were investigated by evaluating the significance of Schottky emission, direct tunneling, and PF tunneling processes to characterize the measured data [49]. Moreover, both the gate and substrate injection conduction mechanisms have also been investigated [50]. In the substrate injection case, the leakage current increases with the increase of the irradiation dose. However, with no electric field, electrons and holes are likely to either recombine, become trapped, or move out of the HfO_2 layer. In the substrate injection case (Fig. 2), the direct tunneling mechanism seems to be dominant in low voltage region up to 1 V as the thickness of the HfO_2 layer is of 5 nm.

The direct tunneling is given by equation [51]

$$J_{DT} = \frac{q^3}{16\pi^2\phi_b}F_{ox}^2\exp\left\{-\frac{4}{3}\frac{\sqrt{2m_{ox}^*}\phi_b^{3/2}}{qF_{ox}}\left[1-\left(1-\frac{qV_{ox}}{\phi_b}\right)^{3/2}\right]\right\} \tag{2}$$

where F_{ox} is the electric field across the oxide, m_{ox}* is the effective electron mass in the oxide, ϕ_b is the barrier height

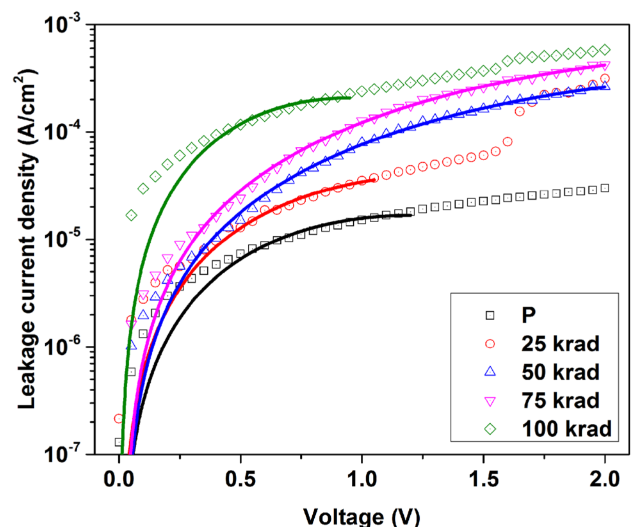

Fig. 2 Leakage current characterized by the direct tunneling mechanism under substrate injection (solid lines indicate fitting)

between conduction bands at the semiconductor–oxide interface, $\hbar$ is the reduced Planck constant, q is the electron charge, and V_{ox} is the voltage across the oxide.

However, as the dose increases, the charge trapping which alters the shape of the I–V characteristics favors the trap-assisted PF tunneling mechanism [52]

$$J_{PF} = EF_{ox}\exp\left[-\frac{q\phi-\beta\sqrt{F_{ox}}}{\xi KT}\right] \tag{3}$$

where K, T, and ξ are constants: Boltzmann's constant, temperature, and a factor that depends on acceptor compensation, respectively (the ξ value is usually between one and two). Figure 3 shows PF tunneling and the linear fitting of ln (J/E) vs. $E^{1/2}$ plots. This analysis suggests that the defect-assisted PF tunneling is predominant as the dose increases and eventually there is an increase in the leakage current. This clearly indicates the increase in the density of oxide traps within the HfO_2 layer. Coming to the gate injection case (shown in Fig. 4a, b), the linear plots ln J vs. $E^{1/2}$ of the pristine and highest gamma dose samples for the electric field $E < 1.5$ MV/cm fit well with the Schottky emission. However, for the electric field $E > 1.5$ MV/cm, the linear plots of $E\times\ln(J/E^2)$ vs. $E^{3/2}$ imply the direct tunneling mechanism. It can be understood as the thickness is low (5 nm HfO_2), the direct tunneling mechanism dominates at $E > 1.5$ MV/cm [50]. The leakage current through the HfO_2 increases with the increase of total dose; this can be attributed to the irradiation-induced EHPs and their transport through HfO_2 layers. The current conduction mechanism of dominance in Schottky emission may be due to the decrease in the interface barrier height with the increase of the irradiation dose, which can be accredited

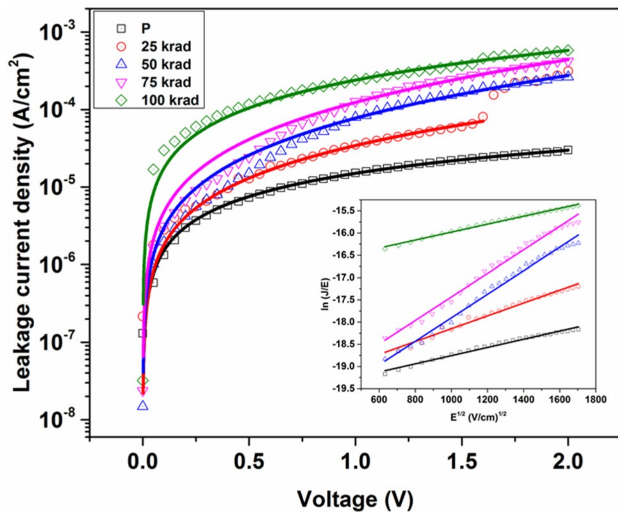

Fig. 3 Leakage current characterized by the PF tunneling mechanism under substrate injection (solid lines indicate fitting); inset: ln(J/E) vs. $E^{1/2}$ plots

to the oxygen vacancy generation and charge trapping in HfO_2 layer.

The defects in HfO_2 may serve as electron and hole traps in these devices. At 1 MHz frequency, these traps are unable to respond to the small AC signal that is applied, and the de-trapping of the trapped charges cannot be accomplished [53]. The trapped charges consequently stay in the HfO_2 films and shift the C–V curve [54]. Figure 5 shows a clear shift in the flat-band voltage and increase in the width of the hysteresis loops as a function of dose. The D_{ot}- and interface-trapped charges (D_{it}) were calculated by the C–V stretch-out method [1] as mentioned in Eqs. 3 and 4 and shown in Table 4

$$D_{ot} = C_{ox} \frac{\Delta V_{MG}}{qA} / cm^2 eV \tag{4}$$

$$D_{it} = C_{ox} \left(\frac{\Delta V_{FB} - \Delta V_{MG}}{qA} \right) / cm^2 eV \tag{5}$$

where D_{ot} is the oxide trap density, D_{it} is the interface trap density, C_{ox} represents the gate oxide capacitance (in accumulation region), ΔV_{FB} is the flat-band voltage, ΔV_{MG} is the midgap voltage, and A is the area (7.85×10^{-3} cm^2).

A shift in the voltage at which the capacitance changes indicates the increase of oxide traps. This shift in flat-band voltage indicates that the majority of the trapped charges are of positive polarity (holes). The reason is that the electrons have higher mobility and may have been swept out from the HfO_2 and leaving holes behind, and therefore, the generated holes are trapped in the oxide layer in which both electron and hole traps are present [55]. The slope of the accumulation region indicates that the interface traps were formed at the interface of HfO_2/Si. The flat-band (ΔV_{FB}) and midgap (ΔV_{MG}) voltage shifts of a C–V curve at 1 MHz frequency with respect to gate voltage suggest that there is an accumulation of oxide- and interface-trapped charges in HfO_2. These shifts are consistent from 25 to 100 krad irradiation dose. Moreover, a change in the interface-trapped charge is evident from the slopes of a C–V plots. Using the changes in the ΔV_{FB} and ΔV_{MG} values, density of oxide (D_{ot})- and interface-trapped charges (D_{it}) were calculated by employing standard analysis methods [56]. The density

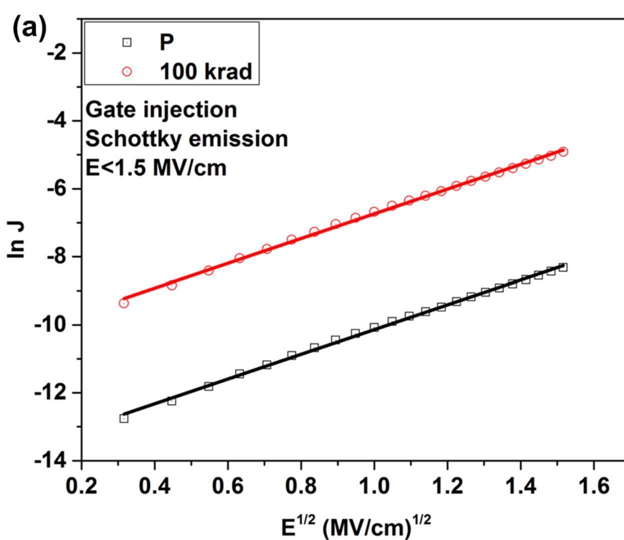

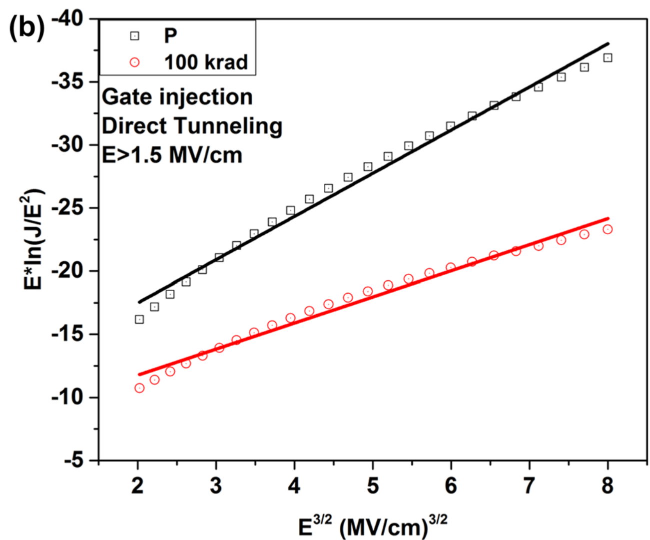

Fig. 4 **a** Conduction mechanism fitting under gate injection for gamma irradiation (ln J vs $E^{1/2}$ for low field $E < 1.5$ MV/cm). **b** Conduction mechanism fitting under gate injection for gamma irradiation (E^* ln(J/E^2) vs $E^{3/2}$ for high field $E > 1.5$ MV/cm)

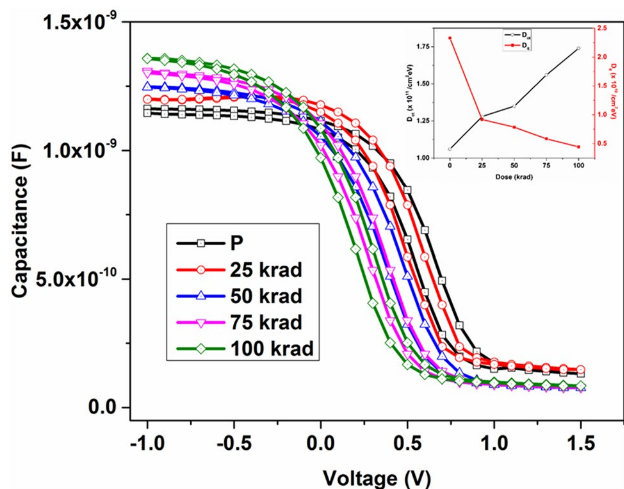

Fig. 5 C–V characteristics at various gamma irradiation doses; inset: changes in oxide-trapped (D_{ot}) and interface-trapped (D_{it}) charge densities of a function of gamma irradiation dose

Table 4 ΔV_{FB}, ΔV_{MG}, D_{it}, and D_{ot} values extracted from C–V characteristics under gamma irradiation

Dose (krad)	ΔV_{FB} (V)	ΔV_{MG} (V)	D_{it} (cm^{-2} eV^{-1})	D_{ot} (cm^{-2} eV^{-1})
P	0.1404	0.1151	2.33×10^{10}	1.06×10^{11}
25	0.1433	0.1337	9.17×10^{9}	1.28×10^{11}
50	0.1442	0.1363	7.84×10^{9}	1.35×10^{11}
75	0.1551	0.1495	5.83×10^{9}	1.56×10^{11}
100	0.1654	0.1613	4.43×10^{9}	1.74×10^{11}

of oxide-trapped charges depends primarily on the number of oxygen vacancies in HfO_2 layer. However, as the dose increases, the number of trapped charges becomes more significant and eventually leads to the shift in the C–V curve. The changes in both the oxide- and interface-trapped charge densities are shown Fig. 5 (inset) as a function of dose. There is an increase in the D_{ot} value from 1.06×10^{11}/cm^{2}eV for pristine to 1.74×10^{11}/cm^2 eV for the 100-krad irradiated samples. However, a decrease in the density of interface charges has been observed. The D_{it} value for pristine sample is estimated to be 2.33×10^{10}/cm^2 eV and it decreases to 4.43×10^{9} /cm^2 eV for 100-krad irradiated sample. This decrease in density of interface states can be attributed to the possible passivation of the Si surface and a decrease in the number of recombination centers in the HfO_2 and HfO_2/Si interfaces.

3.2 SHI irradiation studies

120 MeV Au ion irradiation was performed on the second set of samples and the ion fluence was varied from 1×10^{11} to 5×10^{13} cm^{-2}. The electronic energy loss (S_e), nuclear energy loss (S_n), and the range of 120 MeV Au ions in HfO_2 are estimated to be 24.84 keV/nm, 0.1366 keV/nm, and 8.50 µm, respectively, using SRIM program. In contrast to gamma irradiation, there is a significant change in the structural characterization of the pristine and SHI-irradiated sample (5×10^{13} cm^{-2}) evinced from XRR measurements (See Fig. 6). The thickness and surface/interface roughness are tabulated in Table 3. The composition of HfO_2/Si and HfO_2/HfSiO/Si is expected to vary in the pristine and irradiated samples as a function of fluence. There is a decrease in the thickness of HfO_2 layer (3.89 ± 0.4 nm), and the formation of HfSiO interlayer (2.12 ± 0.6 nm) has been observed at the fluence of 5×10^{13} cm^{-2}. These structural changes can be attributed to SHI-induced intermixing across HfO_2/Si interface. In addition, the thickness of the HfSiO layer has been evolved as there is a contribution from Si substrate also. Moreover, there is an increase surface roughness and interface roughness for the pristine and irradiated samples as tabulated in the Table 3. The structural changes such as phase transitions are also expected in HfO_2 at these fluences [57, 58] which are also expected to affect the electrical properties of HfO_2-based devices.

Figure 7 depicts the I–V characteristics of pristine and SHI-irradiated samples. Similar to the gamma irradiation electrical characterization, i.e., current conduction mechanisms were investigated both in the gate and substrate injection cases. The gate injection case ln J vs. $E^{1/2}$ ($E < 1.5$ MV/cm) and $E \times \ln (J/E^2)$ vs. $E^{3/2}$ ($E > 1.5$ MV/cm)) of SHI-irradiated samples is shown in Fig. 8a and b [50]. From the I–V characteristics of the pristine device, the reduction of leakage current up to 1×10^{12} cm^{-2} can be ascribed to the

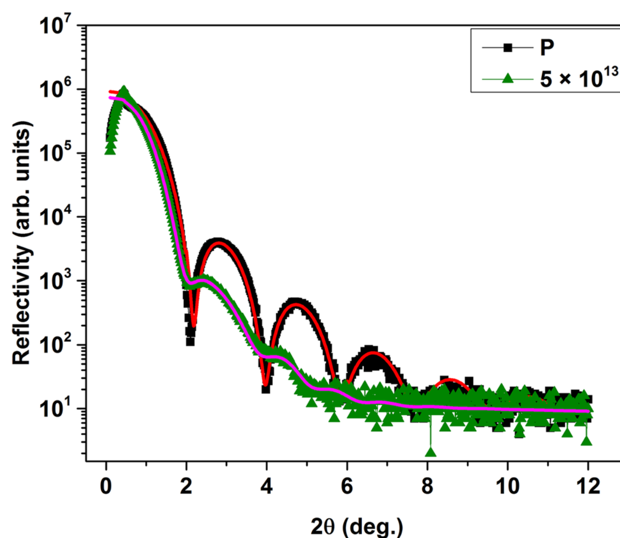

Fig. 6 XRR patterns of pristine and SHI-irradiated (5×10^{13} cm^{-2}) samples (solid lines indicate fitting)

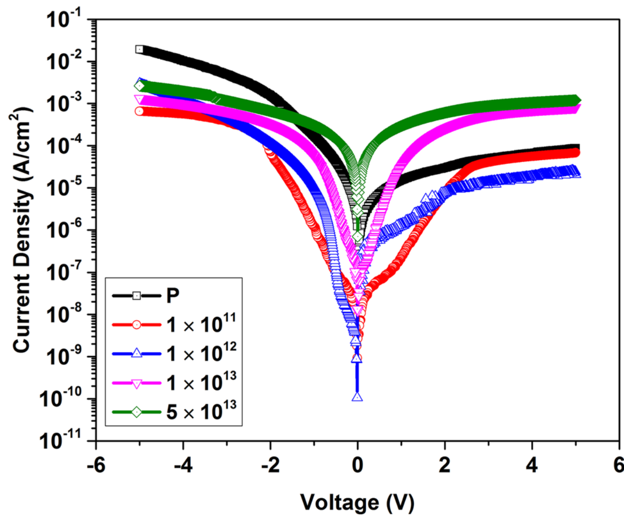

Fig. 7 I–V characteristics of pristine and SHI-irradiated samples

conceivable annealing of defects by electronic excitation due to 120 MeV Au ion irradiation and ultimately improving the device performance which is consistent with our previous study [17]. Above 1×10^{12} cm^{-2} fluence, the leakage current is found to increase for the fluences of 1×10^{13} and 5×10^{13} cm^{-2}. From the I–V characteristics under substrate injection, theoretical fits were performed using direct, FN, and PF tunneling mechanisms and are shown in Fig. 8. Each tunneling mechanism has been examined thoroughly to understand the defect dynamics in view of the observed structural changes. The direct tunneling mechanism is more conspicuous below + 1 V as shown in Fig. 9. Nevertheless, upon irradiation, the leakage current is found to decrease with increase in the irradiation fluence up to a critical fluence of 1×10^{12} cm^{-2}. This can be understood as the SHI annealed out the defects [17, 59, 60]. Moreover, in contrast to gamma irradiation, there is an exponential increase of the leakage current for the fluences 1×10^{11} to 1×10^{13} cm^{-2}. This is due to FN tunneling which dominates at high fields which is given by the following equation [61]

$$J_{\mathrm{FN}} = \frac{q^3}{16\pi^2\phi_{\mathrm{b}}} F_{\mathrm{ox}}^2 \exp\left[-\frac{4}{3}\frac{\sqrt{2m_{\mathrm{ox}}^*}\phi_{\mathrm{b}}^{3/2}}{q}\frac{1}{F_{\mathrm{ox}}}\right] \tag{6}$$

where all the exponential and pre-exponential components are defined earlier.

The transfiguration of the trapezoidal barrier (direct tunneling) of HfO_2/Si into a triangular barrier (FN tunneling) is due to the high electric field, effective mass in the gate dielectric, and barrier height between the HfO_2 and Si [58]. So, the exponential increase of the leakage current developed in the irradiated samples was observed up to a fluence of 1×10^{12} cm^{-2} (see Fig. 10). In case of PF conduction mechanism, the defects can form an energy state near to the conduction/valence band edge depending upon the density of the traps which can restrain the current flow through either capture or emission process. The defect-assisted PF tunneling has been observed not only at 5×10^{13} cm^{-2} fluence but also in the pristine sample itself as the high-k dielectric stack is always composed of oxide/interface defects. The I–V characteristics of the pristine device follow PF tunneling, indubitably representing the presence of traps in the as grown HfO_2. However, the device quality HfO_2 thin films were deposited by ALD, where the density of the interface and oxide traps is expected to be less compared to

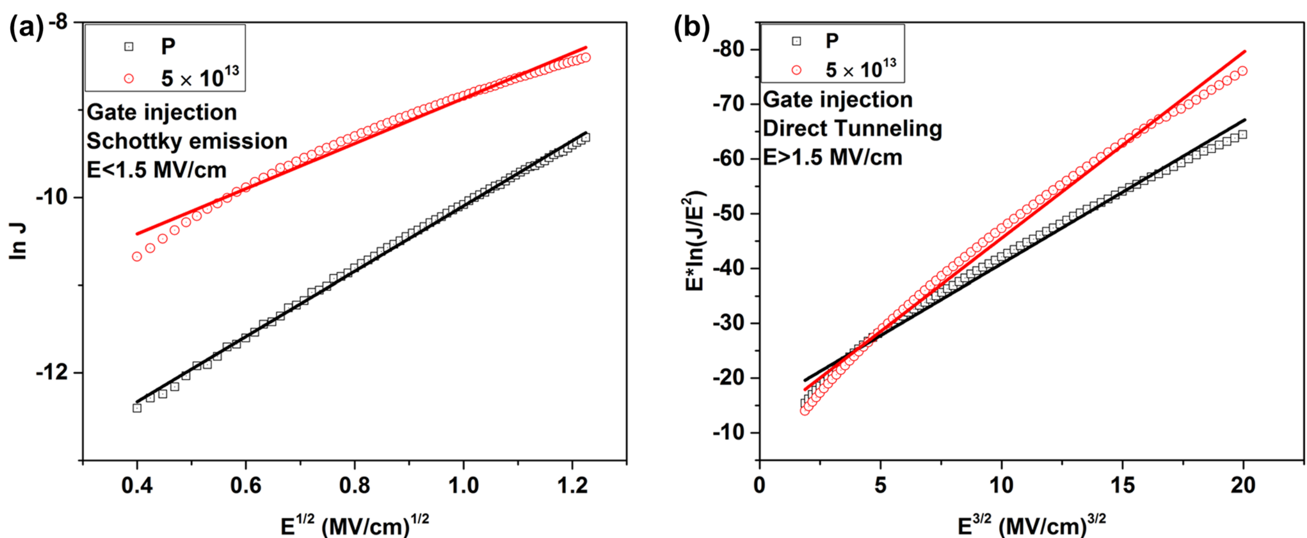

Fig. 8 **a** Conduction mechanism fitting under gate injection for SHI irradiation (ln J vs $E^{1/2}$ for low field $E < 1.5$ MV/cm). **b** Conduction mechanism fitting under gate injection for SHI irradiation (E^* ln(J/E^2) vs $E^{3/2}$ for high field $E > 1.5$ MV/cm)

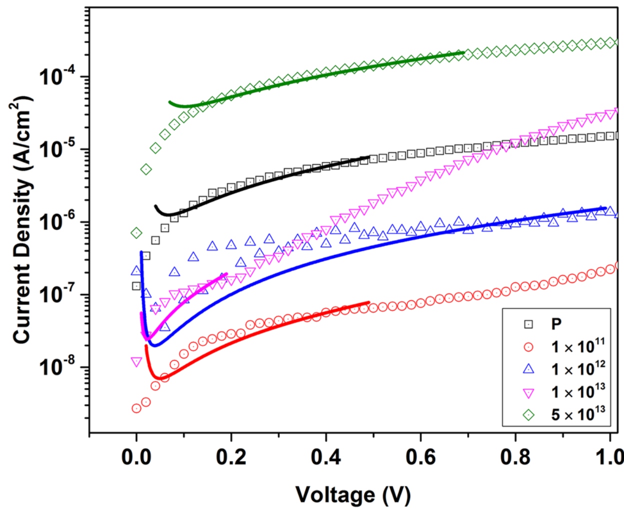

Fig. 9 Leakage current characterized by the direct tunneling mechanism under substrate injection (solid lines indicate fitting)

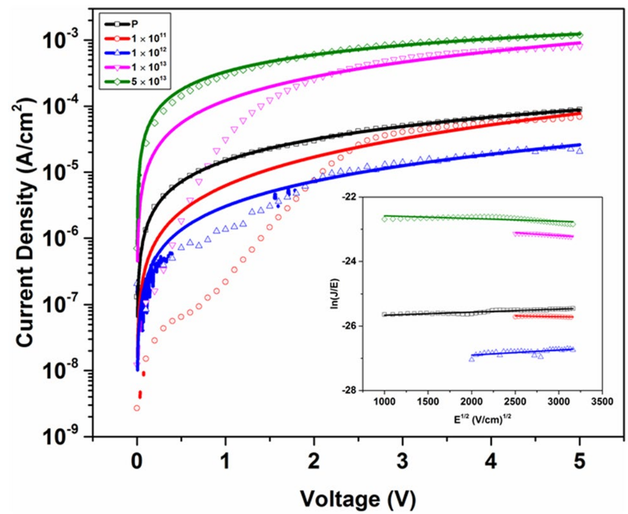

Fig. 11 Leakage current characterized by the PF tunneling mechanism under substrate injection (solid lines indicate fitting); inset: ln(J/E) vs. $E^{1/2}$ plots

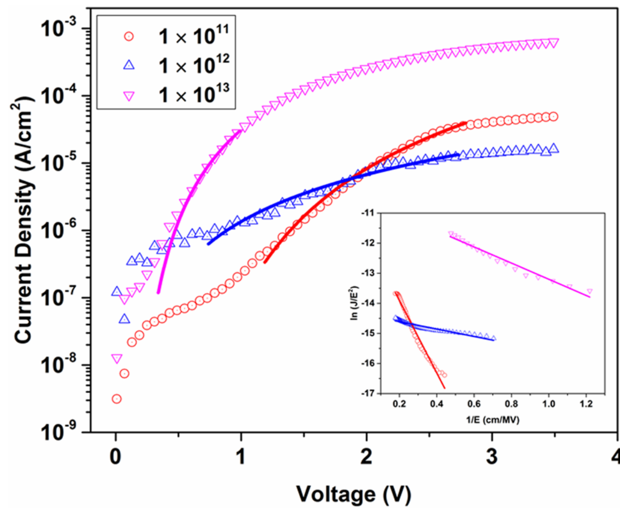

Fig. 10 Leakage current characterized by the FN tunneling mechanism (solid lines indicate fitting); inset: ln(J/E^2) vs. $1/E$ plots

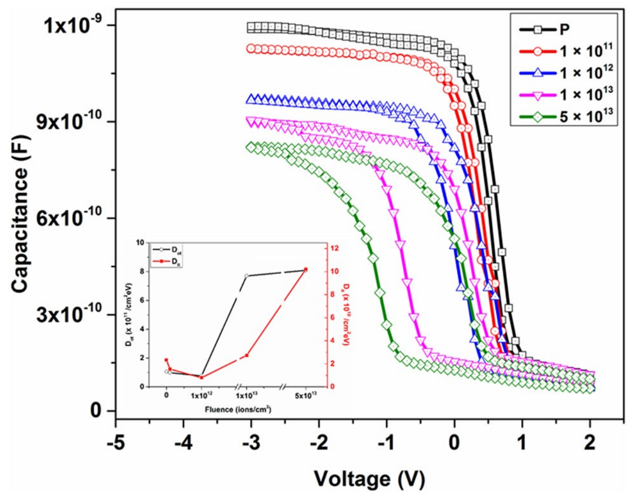

Fig. 12 C–V characteristics at various ion fluences—a decrease in the accumulation capacitance as a function of fluence; inset—changes in oxide-trapped (D_{ot}) and interface-trapped charge (D_{it}) densities as a function of SHI irradiation fluence

any other deposition technique. Beyond a critical fluence of 1×10^{12} cm^{-2}, the creation of defects is substantially high and eventually these defects increased the leakage current (see Fig. 11). However, SHI-induced intermixing effects at higher ion fluences are expected along with the increase in the number of defects. Conversely, the hostile processes of defects creation and the intermixing effects lead to an increase in the leakage current density. The defect creation is mainly due to the atomic displacement during elastic collisions (S_n) of ions with atoms. However, the annealing of defects occurs due to inelastic collisions (S_e) initiating the excitation and ionization of atoms and their subsequent relaxation [17]. After a critical fluence, the damage processes dominate annealing process. These processes are liable for the perceived increase in leakage current at higher ion fluences.

C–V measurements were performed at the frequency of 1 MHz (see Fig. 12). A systematic decrease in the accumulation capacitance with increase in the ion fluence has been observed. This can be attributed to the increase in physical thickness and changes in the composition of the HfSiO interlayer. Moreover, these effects can significantly alter the overall dielectric constant. There is a shift both in the flat-band voltage and in the midgap voltage evinced from the C–V

Table 5 ΔV_{FB}, ΔV_{MG}, D_{it}, and D_{ot} values extracted from C–V characteristics under SHI irradiation

Fluence (cm^{-2})	ΔV_{FB} (V)	ΔV_{MG} (V)	D_{it} (cm^{-2} eV^{-1})	D_{ot} (cm^{-2} eV^{-1})
P	0.1404	0.1151	2.33×10^{10}	1.06×10^{11}
1×10^{11}	0.1218	0.1055	1.54×10^{10}	0.98×10^{11}
1×10^{12}	0.1089	0.0987	0.79×10^{10}	0.76×10^{11}
1×10^{13}	1.1134	1.0753	2.73×10^{10}	7.70×10^{11}
5×10^{13}	1.3926	1.2369	1.02×10^{11}	8.09×10^{11}

characteristics as shown in Table 5. Moreover, the hysteresis loop indicates the enhanced charge trapping process and some positive charges were actually trapped in the oxide. The charge trapping becomes more significant as the width of the hysteresis loop increases as a function of irradiation fluence. This feature may have adverse effects as far as MOS devices are concerned but can have certain advantages for floating gate-based non-volatile memory devices. The data are analyzed to estimate the effects of SHI irradiation on the densities of oxide and interface traps. Hence, these studies help understanding the radiation tolerance of HfO_2-based devices as well as to tailor their properties. The density of interface trapped charges decreases to 0.79×10^{10} from 2.33×10^{11}/cm^2 eV up to 1×10^{12} cm^{-2} and then increases up to 1.02×10^{11}/cm^2 eV. The density of oxide-trapped charges is found to decrease from 1.06×10^{11} to 0.76×10^{11}/cm^2 eV

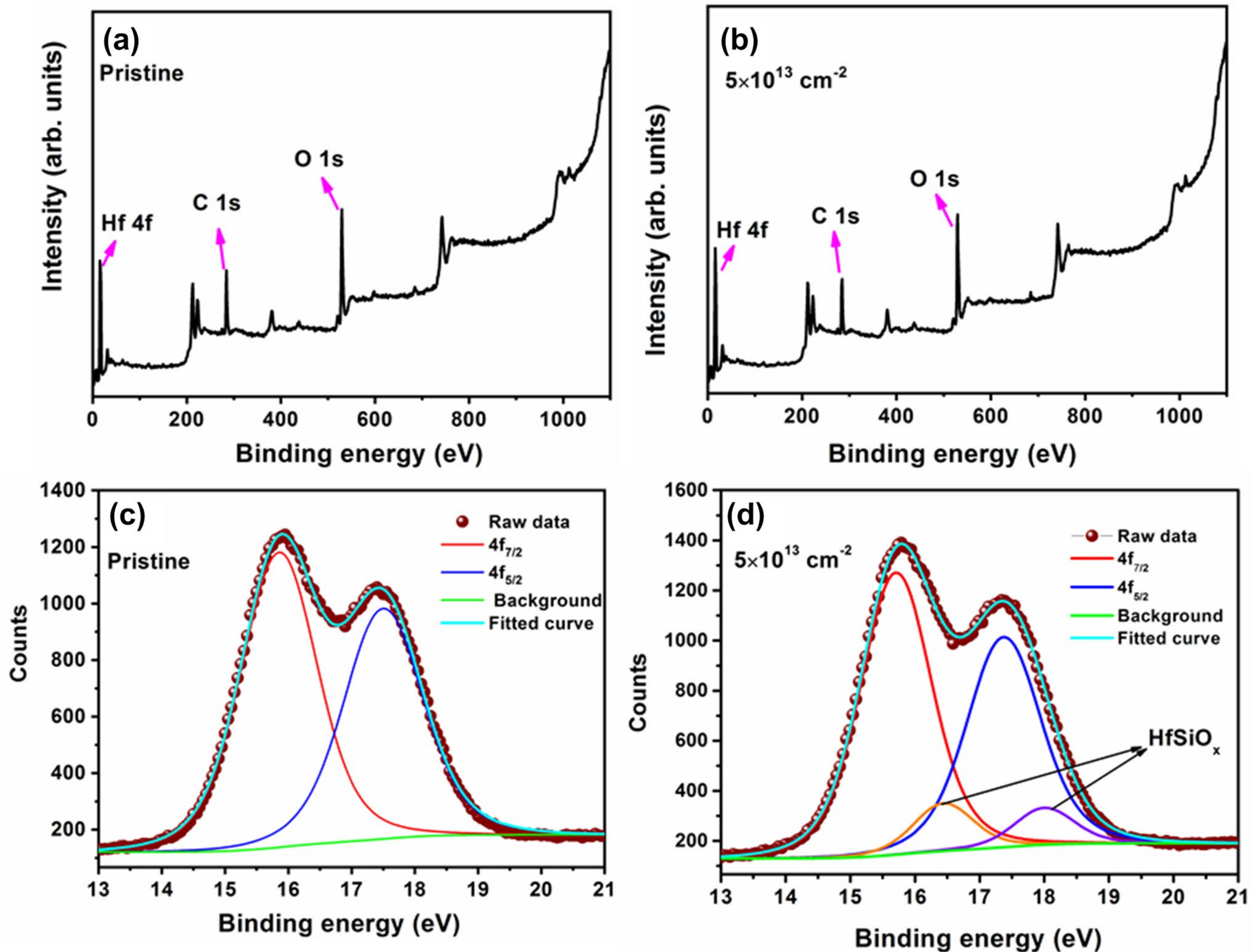

Fig. 13 **a** XPS full-range spectrum of pristine sample; **b** XPS full-range spectrum of SHI-irradiated sample (fluence: 5×10^{13} cm^{-2}); **c** Hf core-level 4f peak of pristine sample; **d** Hf core-level 4f peak of SHI-irradiated sample (fluence: 5×10^{13} cm^{-2})

and then increases up to $8.09 \times 10^{11}/cm^2$ eV as a function of irradiation fluence. As discussed earlier, the density of oxide-trapped charges depends on the number of oxygen vacancies in HfO_2 layer leading to an increase in the charge trapping [62].

In order to analyze the interfacial chemical composition of pristine and ion-irradiated samples, XPS measurements were carried out. Figure 13a and b shows the full scans corresponding to pristine and irradiated samples, respectively. However, to further confirm the existence of $HfSiO_x$ layer at the interface, high-resolution scans of Hf 4f core-level spectra are shown in Fig. 13c and d, respectively. For pristine samples (Fig. 13c), two peaks for Hf $4f_{7/2}$ and Hf $4f_{5/2}$ are found (for pristine and irradiated samples) to be at 15.8 and 17.5 eV (with a spin orbit coupling splitting difference of 1.7 eV), respectively. This can be attributed to the presence of HfO_{2-x} layer in the pristine sample [63]. On the other hand, for ion-irradiated samples (Fig. 13d), Hf $4f_{7/2}$ and Hf $4f_{5/2}$ doublet appears at 15.7 and 17.4 eV, respectively. In addition, two new peaks emerged in the deconvoluted spectra at around 16.3 and 18 eV which can be attributed to the presence of Hf-Si–O bonds [64]. It can be noted that the contribution of the Hf-Si–O bonding after SHI irradiation is 12.5% which cannot be ignored in the present case.

4 Conclusions

The radiation response of Al/HfO_2/Si nMOSCAPs due to both gamma and SHI irradiation has been investigated. XRR measurements of gamma-irradiated samples did not show any significant change in the structural characterization. However, 120 MeV Au ion irradiation yields an evolution of HfSiO interlayer due to high electronic excitation-induced intermixing effects which were confirmed by both XRR and XPS measurements. Both the gamma and the SHI irradiations show significant effects in the oxide and interface trap densities as a function of gamma dose and ion fluence, respectively. Pre-existing defect densities in these devices show substantial effects in charge trapping. Oxygen vacancies are key and responsible reason for the trapping mechanism. Various current conduction mechanisms were investigated in both the gamma and the SHI-irradiated devices. However, the trap-assisted PF tunneling mechanism is more dominant in both the cases. High density of defects and intermixing effects due to SHI irradiation and low-density EHPs produced by gamma irradiation have shown significant effects on the I–V and C–V characteristics. These studies are important to understand the radiation hardness of HfO_2-based devices in order to integrate them in space and nuclear electronic devices.

Acknowledgements We thank Mr. Vinayak Vats, Aixtron Inc., USA, for providing the samples. NMB thanks SERB for fellowship through NPDF scheme (PDF/2016/000748). The financial support and the access to national experimental facilities through collaborative research projects by IUAC, New Delhi, and UGC-DAE-CSR, Kolkata, are greatly appreciated. We thank CFN and UoH for providing access to necessary experimental facilities.

References

1. J. Felix, J. Schwank, D. Fleetwood, M. Shaneyfelt, E. Gusev, Microelectron. Reliab. **44**, 563 (2004)
2. A.H. Johnston, IEEE Trans. Nucl. Sci. **45**, 1339 (1998)
3. H. Jafari, S.A.H. Feghhi, S. Boorboor, Radiat. Meas. **73**, 69 (2015)
4. Y. Mu, C.Z. Zhao, Q. Lu, C. Zhao, Y. Qi, S. Lam, I.Z. Mitrovic, S. Taylor, P.R. Chalker, IEEE Trans. Nucl. Sci. **64**, 673 (2017)
5. P.V. Dressendorfer, J.M. Soden, J.J. Harrington, T.V. Nordstrom, IEEE Trans. Nucl. Sci. **28**, 4281 (1981)
6. J.L. Barth, C.S. Dyer, E.G. Stassinopoulos, IEEE Trans. Nucl. Sci. **50**, 466 (2003)
7. S. Hu, Y. Liu, T. Chen, Q. Guo, Y.-D. Li, X.-Y. Zhang, L.J. Deng, Q. Yu, Y. Yin, S. Hosaka, IEEE Trans. Nanotechnol. **17**, 61 (2018)
8. M.R. Khan, M. Ishfaq, A. Ali, A.S. Bhatti, Mater. Sci. Semicond. Process. **68**, 30 (2017)
9. R. Lok, S. Kaya, H. Karacali, E. Yilmaz, Radiat. Phys. Chem. **141**, 155 (2017)
10. M. Dominguez-Pumar, C.R. Bheesayagari, S. Gorreta, G. Lopez-Rodriguez, J. Pons-Nin, IEEE Trans. Ind. Electron. **65**, 2518 (2018)
11. G.D. Wilk, R.M. Wallace, J.M. Anthony, J. Appl. Phys. **87**, 484 (2000)
12. K.J. Hubbard, D.G. Schlom, J. Mater. Res. **11**, 2757 (1996)
13. M.L. Green, E.P. Gusev, R. Degraeve, E.L. Garfunkel, J. Appl. Phys. **90**, 2057 (2001)
14. S. Campbell, T. Ma, R. Smith, W. Gladfelter, F. Chen, Microelectron. Eng. **59**, 361 (2001)
15. L. Kang, B.H. Lee, W.-J. Qi, Y. Jeon, R. Nieh, S. Gopalan, K. Onishi, J.C. Lee, IEEE Electron Device Lett. **21**, 181 (2000)
16. A. Das, S. Chattopadhyay, G.K. Dalapati, Adv. Mater. Lett. **7**, 123 (2016)
17. N. Manikanthababu, S. Vajandar, N. Arun, A.P. Pathak, K. Asokan, T. Osipowicz, T. Basu, S.V.S. Nageswara Rao, Appl. Phys. Lett. **112**, 131601 (2018)
18. Y. Wang, Z. Lin, X. Cheng, H. Xiao, F. Zhang, S. Zou, Appl. Surf. Sci. **228**, 93 (2004)
19. P.M. Tirmali, A.G. Khairnar, B.N. Joshi, A.M. Mahajan, Solid State Electron. **62**, 44 (2011)
20. L. Pereira, A. Marques, H. Águas, N. Nedev, S. Georgiev, E. Fortunato, R. Martins, Mater. Sci. Eng. B **109**, 89 (2004)
21. K.C. Das, S.P. Ghosh, N. Tripathy, G. Bose, A. Ashok, P. Pal, D.H. Kim, T.I. Lee, J.M. Myoung, J.P. Kar, J. Mater. Sci. Mater. Electron. **26**, 6025 (2015)
22. H. Kim, P.C. McIntyre, K.C. Saraswat, Appl. Phys. Lett. **82**, 106 (2003)
23. S.M. George, Chem. Rev. **110**, 111 (2010)
24. D.M. Hausmann, R.G. Gordon, J. Cryst. Growth **249**, 251 (2003)
25. L. Khomenkova, C. Dufour, P.-E. Coulon, C. Bonafos, F. Gourbilleau, Nanotechnology **21**, 095704 (2010)

26. N. Manikanthababu, T.K. Chan, A.P. Pathak, G. Devaraju, N. Srinivasa Rao, P. Yang, M.B.H. Breese, T. Osipowicz, S.V.S. Nageswara Rao, Nucl. Instrum. Methods Phys. Res. **332**, 389 (2014)
27. N. Manikanthababu, N. Arun, M. Dhanunjaya, V. Saikiran, S.V.S. Nageswara Rao, A.P. Pathak, Radiat. Eff. Defects Solids **170**, 207 (2015)
28. N. Manikanthababu, N. Arun, M. Dhanunjaya, S.V.S. Nageswara Rao, A.P. Pathak, Radiat. Eff. Defects Solids **171**, 77 (2016)
29. N. Manikanthababu, M. Dhanunjaya, S.V.S. Nageswara Rao, A.P. Pathak, Nucl. Instrum. Methods Phys. Res. **379**, 230 (2016)
30. N. Manikanthababu, T.K. Chan, S. Vajandar, V. Saikiran, A.P. Pathak, T. Osipowicz, S.V.S.N. Rao, Appl. Phys. A **123**, 303 (2017)
31. S. Kaya, A. Jaksic, E. Yilmaz, Radiat. Phys. Chem. **149**, 7 (2018)
32. C.Z. Zhao, S. Taylor, M. Werner, P.R. Chalker, R.J. Potter, J.M. Gaskell, A.C. Jones, J. Vac. Sci. Technol. B **27**, 411 (2009)
33. A. Stesmans, V. V. Afanas'ev, F. Chen, S. A. Campbell, Appl. Phys. Lett. **84**, 4574 (2004)
34. D.K. Avasthi, Def. Sci. J. **59**, 401 (2009)
35. S.K. Srivastava, S.A. Khan, P. SudheerBabu, D.K. Avasthi, Nucl. Instrum. Methods Phys. Res. **332**, 377 (2014)
36. H. Amekura, S. Mohapatra, U.B. Singh, S.A. Khan, P.K. Kulriya, N. Ishikawa, N. Okubo, D.K. Avasthi, Nanotechnology **25**, 435301 (2014)
37. S. Verma, K.C. Praveen, A. Bobby, D. Kanjilal, IEEE Trans. Device Mater. Reliab. **14**, 721 (2014)
38. A. Kumar, A. Hähnel, D. Kanjilal, R. Singh, Appl. Phys. Lett. **101**, 153508 (2012)
39. A. Kumar, T. Kumar, A. Hähnel, D. Kanjilal, R. Singh, Appl. Phys. Lett. **104**, 033507 (2014)
40. A. Kumar, J. Dhillon, S. Verma, P. Kumar, K. Asokan, D. Kanjilal, Semicond. Sci. Technol. **33**, 085008 (2018)
41. A. Bobby, N. Shiwakoti, P.M. Sarun, S. Verma, K. Asokan, B.K. Antony, Curr. Appl. Phys. **15**, 1500 (2015)
42. G. Lucovsky, D.M. Fleetwood, S. Lee, H. Seo, R.D. Schrimpf, J.A. Felix, J. Lning, L.B. Fleming, M. Ulrich, D.E. Aspnes, IEEE Trans. Nucl. Sci. **53**, 3644 (2006)
43. V.S. Vendamani, Z.Y. Dang, P. Ramana, A.P. Pathak, V.V. RaviKanthKumar, M.B.H. Breese, S.V.S. Nageswara Rao, Nucl. Instrum. Methods Phys. Res. **358**, 105 (2015)
44. N. Fairley, A. Carrick, J. Walton, P. Wincott, *Peak Fitting with CasaXPS* (Accolyte Science, Knutsford, 2010)
45. G.P. Summers, E.A. Burke, P. Shapiro, S.R. Messenger, R.J. Walters, IEEE Trans. Nucl. Sci. **40**, 1372 (1993)
46. J.H. Cahn, J. Appl. Phys. **30**, 1310 (1959)
47. J.F. Ziegler, M.D. Ziegler, J.P. Biersack, Nucl. Instrum. Methods Phys. Res. **268**, 1818 (2010)
48. S. Daniel, Study of the degradation process of polyimide induced by high energetic ion irradiation, Universität Marburg (2008)
49. Y. Seo, S. Lee, I. An, C. Song, H. Jeong, Semicond. Sci. Technol. **24**, 115016 (2009)
50. H. Wang, Y. Wang, J. Zhang, C. Ye, H.B. Wang, J. Feng, B.Y. Wang, Q. Li, Y. Jiang, Appl. Phys. Lett. **93**, 202904 (2008)
51. K.Y. Cheong, J.H. Moon, H.J. Kim, W. Bahng, N.-K. Kim, J. Appl. Phys. **103**, 084113 (2008)
52. A. Paskaleva, A.J. Bauer, M. Lemberger, S. Zürcher, J. Appl. Phys. **95**, 5583 (2004)
53. Y. Wang, H. Wang, C. Ye, J. Zhang, H. Wang, Y. Jiang, A.C.S. Appl, Mater. Interfaces **3**, 3813 (2011)
54. E. Yilmaz, B. Kaleli, R. Turan, Nucl. Instrum. Methods Phys. Res. **264**, 287 (2007)
55. S. Kaya, E. Yilmaz, J. Radioanal. Nucl. Chem. **302**, 425 (2014)
56. J.L. Gavartin, D. MuñozRamo, A.L. Shluger, G. Bersuker, B.H. Lee, Appl. Phys. Lett. **89**, 082908 (2006)
57. A. Benyagoub, Phys. Rev. B **72**, 094114 (2005)
58. M. Dhanunjaya, D.K. Avasthi, A.P. Pathak, S.A. Khan, S.V.S. Nageswara Rao, Appl. Phys. A **124**, 587 (2018)
59. D.C. Agarwal, F. Singh, D. Kabiraj, S. Sen, P.K. Kulariya, I. Sulania, S. Nozaki, R.S. Chauhan, D.K. Avasthi, J. Phys. D. Appl. Phys. **41**, 045305 (2008)
60. Y. Zhang, R. Sachan, O.H. Pakarinen, M.F. Chisholm, P. Liu, H. Xue, W.J. Weber, Nat. Commun. **6**, 8049 (2015)
61. J.C. Ranuárez, M.J. Deen, C.-H. Chen, Microelectron. Reliab. **46**, 1939 (2006)
62. R.G. Southwick, W.B. Knowlton, IEEE Trans. Device Mater. Reliab. **6**, 136 (2006)
63. S.U. Sharath, T. Bertaud, J. Kurian, E. Hildebrandt, C. Walczyk, P. Calka, P. Zaumseil, M. Sowinska, D. Walczyk, A. Gloskovskii, T. Schroeder, L. Alff, Appl. Phys. Lett. **104**, 063502 (2014)
64. J.W. Zhang, G. He, M. Liu, H.S. Chen, Y.M. Liu, Z.Q. Sun, X.S. Chen, Appl. Surf. Sci. **346**, 489 (2015)

Publisher's Note Springer Nature remains neutral with regard to jurisdictional claims in published maps and institutional affiliations.